Fabrication and performance optimization of an advanced pervaporation desalination membrane: A study utilizing PVDF and hydrophilic active layer as composite

Thi Thi Mar [a], Yunlong Xue [a], Yu Chang [b], Zijian Yu [b], Zhongxiao Du [b], Bing Cao [b,**], Rui Zhang [b,c,*]

[a] College of Materials Science and Engineering, Beijing University of Chemical Technology, Beijing, 100029, China
[b] Engineering and Technology Research Center of Membrane for Chemical Industry , College of Chemical Engineering, Beijing University of Chemical Technology, Beijing, 100029, China
[c] National-Local Joint Engineering Research Center Of Biomass Refining and High-Quality Utilization, Changzhou 213164, China

ARTICLE INFO

ABSTRACT

Pervaporation emerges as a promising technique for brine treatment. In this investigation, we employed a PVDF substrate layer and applied various coating solutions using a simple spray technique to produce a composite pervaporation membrane. The composite membrane's chemical structure, morphology, hydrophilicity, swelling property, surface roughness, and crosslinking conditions were thoroughly investigated. Notably, the PVDF/PEI/P (SS-MA) composite membrane exhibited outstanding desalination performance, demonstrating high salt rejection and flux of 308.7 ± 13.8 kg m^{-2} h^{-1} when subjected to a 3.5 wt% sodium chloride solution. Even at an elevated brine concentration of 20 wt%, the membrane maintained a commendable flux of 88.76 ± 5.4 kg m^{-2} h^{-1} at 72 °C. These findings underscore the efficacy of the developed composite membrane for brine desalination applications.

1. Introduction

The persistent global challenge of water scarcity remains a significant impediment to progress [1–3]. Desalination of saltwater, encompassing both brackish water and seawater, emerges as a compelling solution to this issue [4–7]. Among desalination technologies, membrane-based methods are pivotal due to their high separation efficiency, low energy consumption, and facile production [8,9]. Reverse osmosis constitutes over 65 % of freshwater production from brackish and saltwater, primarily due to its higher water yield at a relatively low cost [10–12]. However, the escalating salt concentration in brine necessitates higher operating pressures for reverse osmosis desalination, leading to reduced production rates and increased energy costs [13,14]. In the pursuit of desalinating highly salinized water, pervaporation, an efficient and cost-effective membrane technology, has gained significant attention and rapid development [15]. Composite membranes, typically featuring a dense hydrophilic layer in pervaporation applications, exhibit ultrahigh salt rejection and resistance to fouling [7,16,17]. The

permeation of water through the membrane and subsequent vaporization on the permeate side results in a high-quality product, effectively preventing the passage of other volatile substances and potentially harmful solutes [2,10,18]. Consequently, regulating the permeability of a pervaporation membrane becomes the main point among the researchers. Exemplary studies showcase advancements in pervaporation membrane design and performance. Meng et al. fabricated a PVA-SBQ/NC-PAN composite membrane, achieving a permeation rate of 122.6 ± 10.8 kg m^{-2} h^{-1} while desalinating a 3.5 wt% NaCl solution at 75 °C [19]. Utilizing PVDF-based composite membranes, F.U. Nigiz and N. D. Hilmioglu treated seawater by increasing the water flux to 1.6 kg m^{-2} h^{-1} at 60 °C [20]. The PVA/PVDF composite membrane was prepared using the non-solvent-induced phase inversion process for pervaporation desalination, as reported by Qin et al. When a 3.5 wt% NaCl solution was desalinated at 70 °C, the permeation rate was released at 70.4 ± 2.5 kg m^{-2} h^{-1} [21]. For pervaporation desalination, Zhao et al. constructed the PVA-FS/PVDF composite membrane. Using a 3.5 wt% NaCl solution, they were able to further increase the water flux to

---

34 ± 1 kg m^{-2} h^{-1} while maintaining a 99.93 % salt rejection at 70 °C [22]. Notably, Xue et al. observed composite pervaporation desalination membranes with the highest water flux, underscoring the significance of membrane-supporting and active layers in designing pervaporation composite membranes with superior water flux [23]. A PVA coating solution with a P(AA-AMPS) crosslinker on the PTFE supporting layer demonstrated a high flux value of 256.6 ± 31.3 kg m^{-2} h^{-1} at 75 °C, according to Wang et al. [24]. A composite membrane was created by Zhao et al. using an FS-3100 crosslinker on the PVDF supporting layer and a dense polyvinyl alcohol (PVA) layer [22]. The PSF composite membrane was created by Qin and colleagues utilizing a PVA coating solution with a P(AA-AMPS) crosslinker, exhibiting a flux value of 124.8 ± 3.2 kg m^{-2} h^{-1} [25]. As a consequence, in this experiment, we employed PVA and PEI with P(SS-MA), SPTA, P(AA-AMPS), and TMC materials as crosslinking agents, along with other hydrophilic coating solutions. PVA coating solution containing P(SS-MA), SPTA, and P(AA-AMPS) crosslinkers demonstrated the ester linkage, while the amide linkage was demonstrated by PEI coating solution containing P(SS-MA), and TMC.

This study spearheaded the creation of an exceptional pervaporation membrane designed for desalination, leveraging polyvinylidene fluoride (PVDF) as the substrate layer material and incorporating diverse active layers. Notably, the PVDF membrane with PEI/P(SS-MA) surpassed its counterparts in flux values, demonstrating superior performance. The PVDF/PEI/P(SS-MA) composite, characterized by a minimal fouling tendency, stands out as the top-performing membrane for water separation. These results underscore that the heightened hydrophilicity achieved on the PVDF substrate membrane surface is the fundamental catalyst driving the observed enhancement in permeation flux within the composite membrane.

2. Experimental

2.1. Materials

Poly (vinylidene fluoride) (PVDF, purity ≥99.5 %, M$_w$: 200,000), Poly(vinylpyrrolidone) (PVP K-30, purity ≥95.0 %, M$_w$: 50,000) and poly (4-styrenesulfonic acid-co-maleic acid) sodium salt (P(SS-MA), M$_w$: 20,000) were bought from Gobekie Co., Ltd. Polyethylene terephthalate non-woven fabric paper was purchased from Shanghai Pole Technology Co., Ltd. Poly (vinyl alcohol) (PVA, hydrolysis degree: 99.4 %, M$_w$: 105,000), N-methyl-2-pyrrolidone (NMP, purity ≥99.0 %), and 98 % sulfuric acid (H$_2$SO$_4$) were supplied from Tianjin Fuyu Fine Chemical Reagent Factory (China). Sodium chloride (NaCl, purity ≥99.5 %) was bought from Sinopharm Chemical Co., Ltd. (China). We purchased 4-sulfophthalic acid (SPTA), poly acrylic acid co-2-acrylamido-2-methyl propane sulfonic acid (P(AA-AMPS), M$_w$: 2000–5000 g mol^{-1}), trimesoylchloride (TMC, purity ≥98 %) and ethyleneimine polymer (PEI, purity ≥99 %, M$_w$: 600) from Shandong Usolf Chemical Technology Co., Ltd. Sodium alginate (SA, M$_w$: 270,000 g mol^{-1}) and sodium dodecyl benzene sulfone (SDBS, M$_w$: 348.48, purity: 98 %) were obtained from Aladdin Co., Ltd. (China) and Tween 20 (M$_w$: 1227.5, boiling point: 110 °C) was received from Tianjin Guang Fu fine chemical research institute (China). A Millipore ultrapure water system that was set up in our lab provided deionized (DI) water.

2.2. Preparation of thin film composite membranes

2.2.1. Preparation of PVDF substrate layer

The non-solvent-induced phase inversion technique was employed to create the PVDF membranes. Initially, a homogeneous solution comprising PVDF and PVP polymers dissolved in NMP was prepared, with the mass ratios of the three components being 20/4/100 respectively. To ensure the elimination of air bubbles, the solution was left to settle overnight. Subsequently, a casting knife was utilized to apply the PVDF substrate layers onto PET non-woven fabric paper, maintaining a consistent substrate layer thickness of 200 μm. The PVDF membranes were then immersed in a coagulation bath containing deionized water for approximately three days to remove any residual solvents. The deionized water in the coagulation bath was replaced with fresh deionized water every 12 h to ensure thorough solvent removal. After the immersion period, the PVDF membranes were removed from the coagulation bath and left to air dry at room temperature. The process for fabricating the substrate layer is illustrated in Fig. 1.

2.2.2. Spray-coating and post-cross-linking processes

Initially, the PVDF membrane with an effective area of 3.5 cm × 3.5 cm was affixed onto a glass plate using moisture-resistant membrane jointing tape. Using the airbrush compressor, the coating solution was applied perpendicularly at a distance of 150 mm to the PVDF membrane's surface. The crosslink was created by placing the composite membrane in the muffle oven after spraying for 15 min at 100 °C. The preparation of the composite membrane is shown in Fig. 2. The compositions of the substrate layer and coating layer are described in Table 1.

2.3. Characterization of membrane

2.3.1. Chemical structural analysis

The chemical structure of the composite membranes was characterized by Fourier transform infrared spectroscopy (ATR-FTIR, Nicolet 560, ThermoScientific, Japan) to investigate the chemical structures of the membranes with different crosslinkers. (see Table 2)

2.3.2. Morphological examination

Cross-section and surface morphologies of membranes were characterized by a scanning electron microscope (SEM) (HITACHI S-7800, Japan). Cross-sectional micrographs were obtained from composites fractured in liquid nitrogen and the membranes were cut with a blade. The average pore size and surface porosity of the PVDF membranes were determined based on the SEM image using Image J software. The surface roughness of the membranes was analyzed using the atomic force microscope (AFM, Dimension Fastscantm, Bruker, USA). The surface roughness value of the membranes was calculated using the Gwyddion - SPM data analysis software.

2.3.3. Thermal analysis

Thermogravimetric analysis (TGA) equipment (instrument model TA Q100, TA Instrument, USA) was used to determine the thermal properties of the prepared samples at various temperatures ranging from room temperature to 600 °C at a heating rate of 10 °Cmin^{-1} in an inert nitrogen atmosphere. Before TGA testing, the film samples suffered a thermal treatment in a vacuum at 40 °C.

2.3.4. Hydrophilicity assessment

A Contact Angle Goniometer (DSA 100, KRUSS, Germany) was used to know the membranes' water contact angles. A droplet of deionized water was set on the membrane surface and determined using the Contact Angle Goniometer device. To obtain the average value of the water contact angle, measurements were taken at least five times for
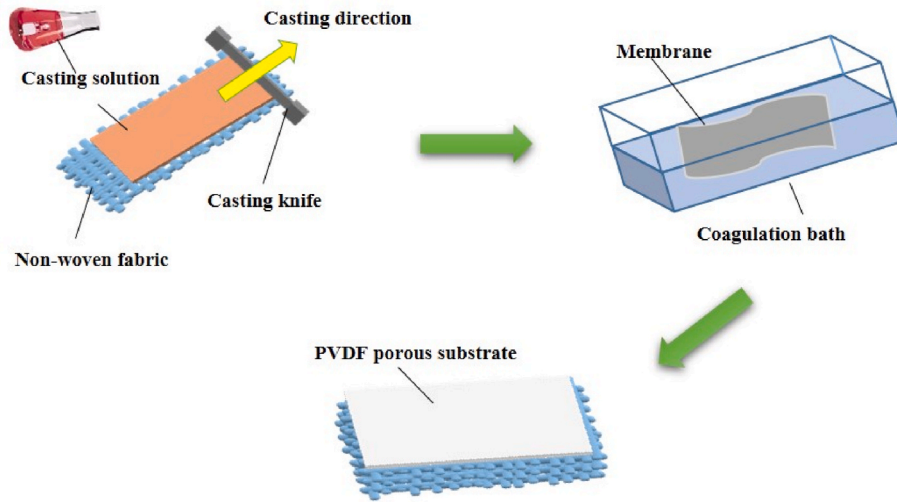
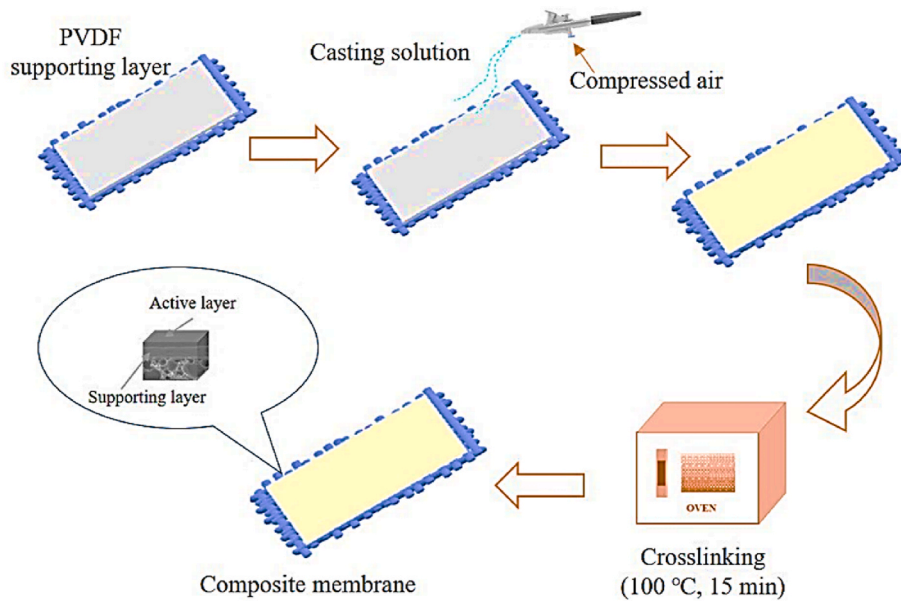**Fig. 1.** Preparation protocol of PVDF substrate membrane.

Fig. 2. Preparation protocol of PVDF composite membrane.

Table 1
Composition of the PVDF substrate layer and coating layer.

Substrate layer	Weight ratio (wt.%: wt.%)	Coating layer	Weight ratio (wt.%: wt.%)	Spray amount (μm)
PVDF/PVP/ NMP	20:4:100	PVA/P(AA-AMPS)	1.5:30	600
PVDF/PVP/ NMP	20:4:100	PVA/SPTA	1.5:10	600
PVDF/PVP/ NMP	20:4:100	PVA/P(SS-MA)	1.5:30	600
PVDF/PVP/ NMP	20:4:100	PEI/TMC	1:0.3	600
PVDF/PVP/ NMP	20:4:100	PEI/P(SS-MA)	1:30	600

Table 2
Swelling degree of films NaCl concentration from 0 wt% to 10 wt%.

Sample	Thickness (mm)	Swelling degree (%)	
		0 wt % NaCl	10 wt % NaCl
PVA	0.038	dissolve	103.7 ± 7.2
PVA/P(SS-MA)	0.046	dissolve	138.2 ± 11.1
PVA/P(AA-AMPS)	0.031	dissolve	77.1 ± 5.6
PVA/SPTA	0.028	297.4 ± 13.1	112.5 ± 8.3
PEI/TMC	0.203	300.4 ± 13.4	142.5 ± 11.2
PEI/P(SS-MA)	0.196	335.5 ± 15.1	112.3 ± 9.4

to solvent exchange with deionized water and a 10 wt% sodium chloride solution repeatedly. Excess water was carefully removed from the membrane surface using thin paper before weighing the wet weight of these membranes. Equation (1) was then employed to calculate the water absorption of both the crosslinked membrane and the substrate.

each sample.

Water absorption measurements of the membranes were initially dried in a vacuum at 60 °C for 24 h to determine the dry weight. Subsequently, the dried membranes were wetted with alcohol and subjected

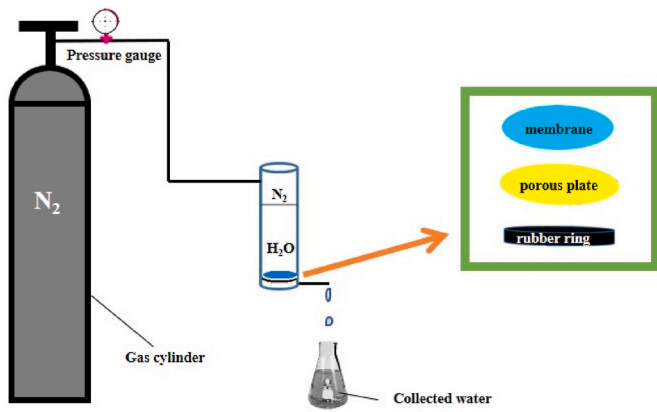$$SD = \frac{W_w - W_d}{W_d} \times 100\% \qquad (1)$$

Fig. 3. The diagrammatic sketch of the ultrafiltration device.

where W_w and W_d represent the mass of the swollen and dried membrane sample, respectively, in grams.

2.3.5. Determination of the pure water flux

The ultrafiltration testing device was used to measure the pure water flux of the membrane. A schematic diagram is shown in Fig. 3. Firstly, the membrane was placed on top of the membrane cell and 0.3 MPa pressure of nitrogen gas was used to remove any gas for 30 min. Then the pressure was reduced to 0.1 MPa and pure water flux was tested. The pure water flux was calculated using the following equation (2).

$$J = \frac{M}{A_1 \times T_1} \tag{2}$$

where T_1 was the operating period (h), A_1 was area of membrane (m^2), J was flux value of water (kg m^{-2} h^{-1}), and M was the weight of collected water (kg).

2.3.6. Gas permeation test of the PVDF substrate membrane

To investigate the relationship between trans-membrane pressure and gas flux, as well as to calculate the membrane's resistance to water vapor permeation, a laboratory-made gas permeation cell (CAT.NO. XX4404700, MIL.LIPORE CORP., Japan) was used. The schematic diagram of the experimental setup is provided in Fig. 4. The fluxes of N_2 and CO_2 were calculated using equation (3).
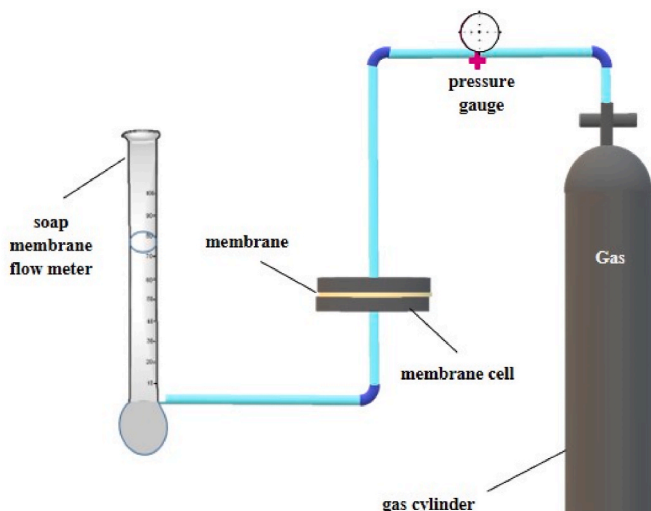
$$Q = \frac{V}{A \times T} \tag{3}$$

where V was the permeable gas volume (L), A was the effective membrane area (m^2), T was the operation time (h), and Q was the gas flux (L m^{-2} h^{-1}).

2.3.7. Pervaporation test

The desalination properties of the composite membranes were measured using the bespoke equipment shown in our previous work [21]. The feed solution was heated to operating temperature before the pervaporation process, and it was then brought into contact with the feed side of a nonporous membrane. The permeating substance occasionally passes through the membrane and is continuously eliminated from the permeate side of the membrane in the form of water vapor. Hydrophilic dense membranes perform as an inhibitor in the pervaporation process among the liquid phase of the feed salt solution and the vapor phase of the permeate solution to produce fresh water. The membrane permeate side was maintained under a vacuum of 100 Pa and permeate water vapor was collected by a liquid nitrogen cold trap. The effective membrane area was 3.14 cm^2 and the operation was carried out four times, each time taking 10 min. Using a DDSJ-308F electrical conductivity meter (Leichi, China), feed concentration and permeate concentration were calculated. The flux value (J) was calculated using the following equation (4).

$$J = \frac{M}{s_1 \cdot t_1} \tag{4}$$

where J was the water flux value (kg m^{-2} h^{-1}), s_1 was the effective membrane area (m^2), M was the water volume collected by the cold trap through the permeate side (kg), and t_1 was the operation time (h). Salt rejection (R_{NaCl}, %) of sodium chloride was measured using the following equation (5).

$$R_{NaCl} = \frac{C_{feed} - C_{permeate}}{C_{feed}} \times 100\% \tag{5}$$

where C_{feed} was the salt concentration of the feed solution (m S cm^{-1}) and $C_{permeate}$ was the salt concentration of the permeate solution (m S cm^{-1}).
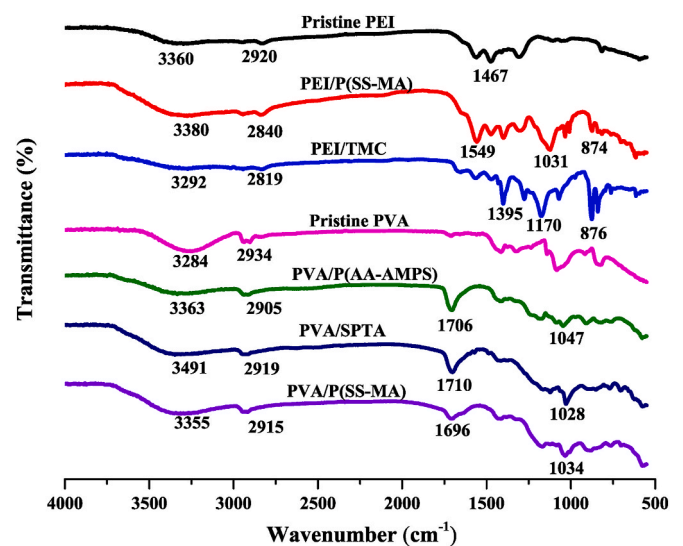

Fig. 4. The diagrammatic sketch of gas permeation cell.

Fig. 5. FTIR spectrum of PVDF composite membranes using PEI and PVA coating solution with different crosslinkers.

3. Results and discussion

3.1. Characterization of crosslinking reactions

For pristine PEI, the broad peak at around 3360 cm^{-1} corresponds to the N–H stretching vibrations, while the C–H stretching is observed near 2920 cm^{-1}, moreover, for pristine polyvinyl alcohol (PVA), the FTIR spectrum reveals a broad absorption peak around 3284 cm^{-1}, indicative of OH stretching vibrations from hydroxyl groups. The peak observed at approximately 2934 cm^{-1} corresponds to C–H stretching vibrations. Additionally, a distinct peak at around 1050 cm^{-1} is attributed to C–O stretching vibrations. The C–N stretching vibration appears at 1467 cm^{-1}. P(SS-MA), P(AA-AMPS), and SPTA were found to crosslink PVA in the FTIR spectrum (Fig. 5). Two significant peaks can be used to explain this: the duplet absorption peaks (CH stretching), which occurred at 2800 cm^{-1} to 2950 cm^{-1}, and the OH stretching frequency, v = 3300 cm^{-1} to 3400 cm^{-1}. This finding indicates that hydrogen bonds between the OH groups of PVA and the crosslinkers have taken place. Since the carbonyl group of COOH in crosslinkers did not completely react with the OH groups of the PVA chain, the C=O band was between 1600 cm^{-1} and 1700 cm^{-1}. For PEI coating solution with P(SS-MA) and TMC crosslinkers, a wider C–N stretching frequency of aliphatic amide occurred from 1000 to 1150 cm^{-1}. N–H wagging bands of amide occurred at 870 cm^{-1} to 880 cm^{-1}. About 1400 cm^{-1} showed the C–N stretching vibration. The duplet absorption peak (CH stretching) occurred at 2800 cm^{-1} to 2900 cm^{-1}. The C–O stretching frequency decreased to 1500 cm^{-1} because the amide bond was formed between PEI and crosslinkers. The amide linkage of PEI and P(SS-MA) on the

PVDF supporting layer was one of the factors to get a higher flux value than other linkages. Moreover, Fig. 6 illustrates the crosslinking reaction of coating polymers with different crosslinkers.

3.2. Comparative analysis of selected crosslinking systems for PVA and PEI

Thermogravimetric analysis (TGA) in a nitrogen atmosphere has been used to examine the thermal stability of films made of pristine PVA, PVA with different crosslinkers (P(AA-AMPS), P(SS-MA), SPTA) and PEI with two kinds of crosslinker such as P(SS-MA) and TMC. Three breakdown phases can be seen in PVA, PEI/P(SS-MA), PVA/P(AA-AMPS), and PVA/SPTA films, but only two can be seen in PVA/P(SS-MA) and PEI/TMC (Fig. 7). PVA/P(AA-AMPS) and PVA/SPTA films exhibit nearly comparable total weight losses (almost 60 %), according to TGA thermograms in a nitrogen environment, but pristine PVA and PVA/P(SS-MA) films exhibit nearly identical weight losses (almost 80 %). This result suggests that they both have equal thermal stability. In comparison to PVA/P(AA-AMPS) and PVA/SPTA films. PVA/P(SS-MA) films lost more weight in the first stage, according to TGA curves. Water was released as a result of additional interactions between P(SS-MA)'s –COOH groups and PVA's –OH groups. The release of water during esterification and amide reactions involving the OH functional groups of PVA and COOH, NH$_2$ functional groups of SPTA, P(AA-AMPS), and P(SS-MA), and OH functional groups of P(AA-AMPS) is responsible for the weight loss in films [2,26]. The first stage's lower weight percentage losses, which took place between 40 °C and 100 °C, were attributed to the physically absorbed water molecules evaporating from
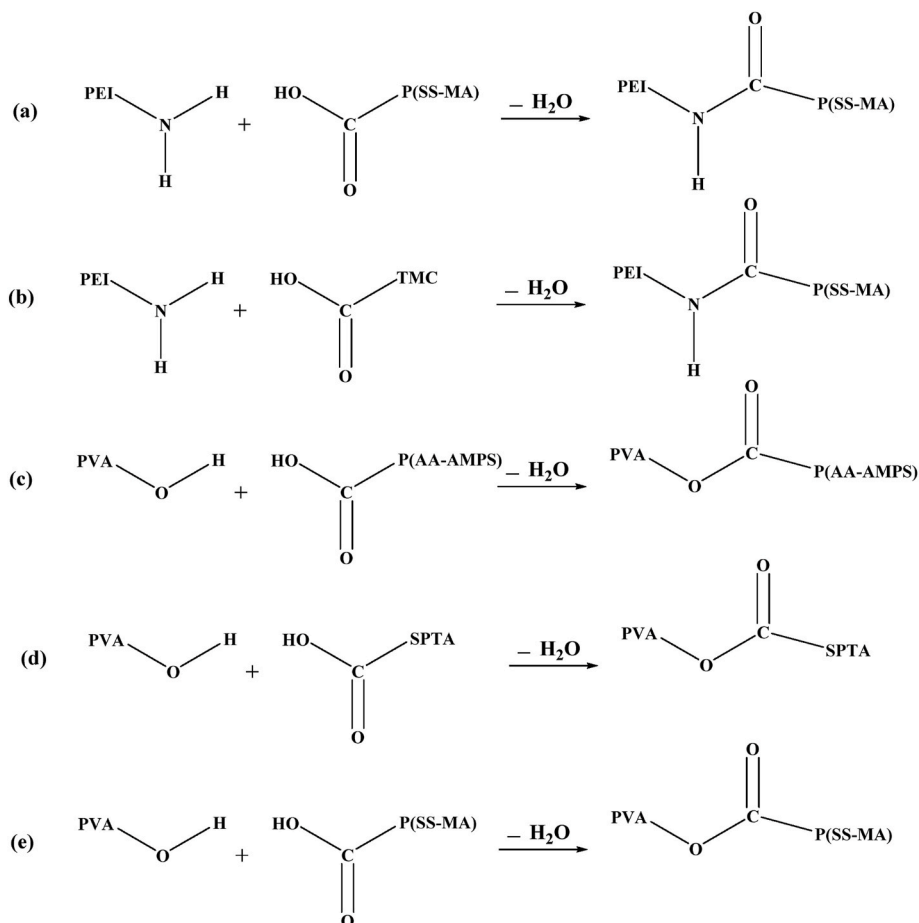

Fig. 6. Crosslinking reactions of PEI and PVA coating solution with different crosslinkers such as P(AA-AMPS), SPTA, P(SS-MA), and TMC.
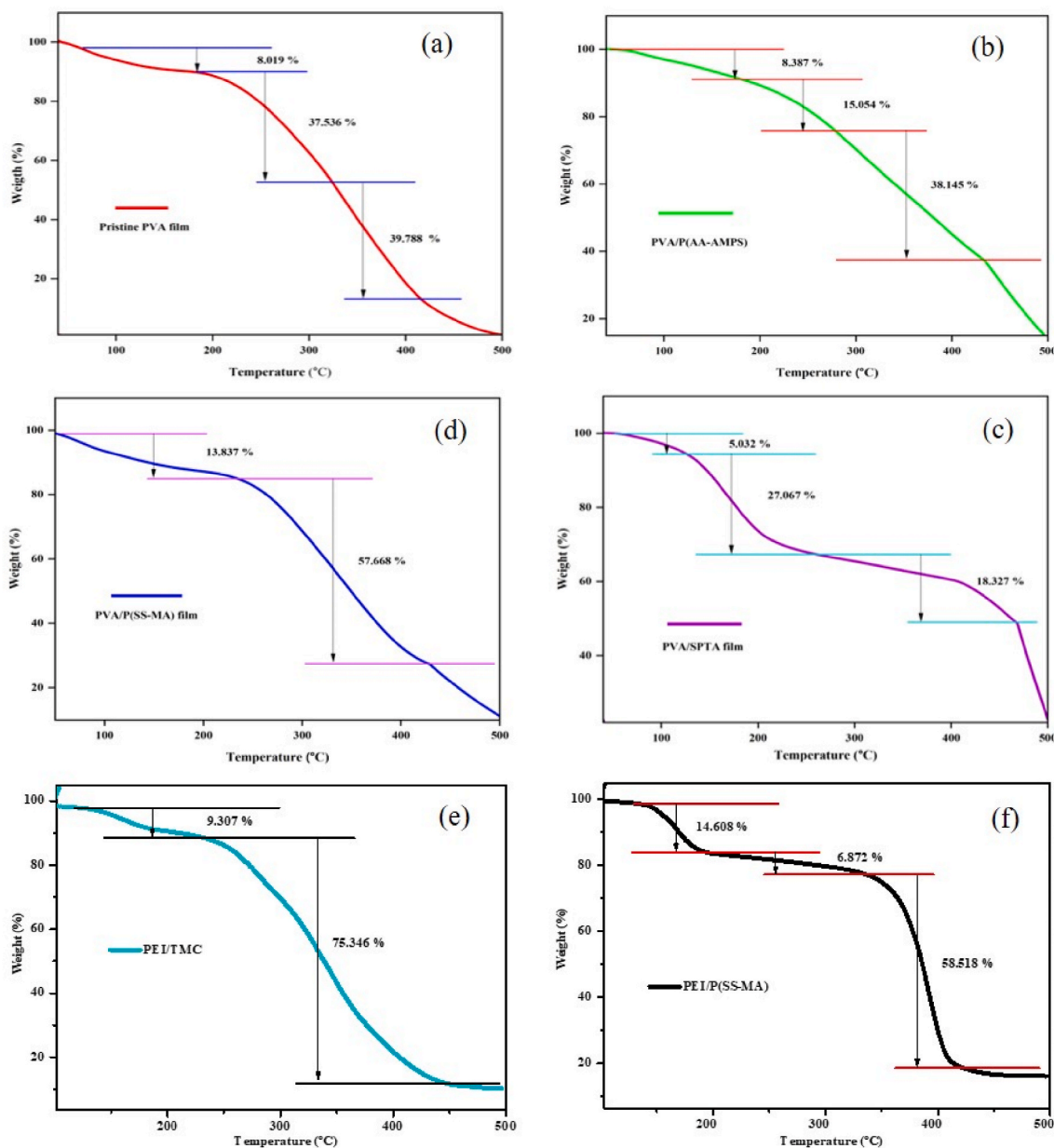
Fig. 7. TGA curves of films (a) PVA, (b) PVA/P(AA-AMPS), (c) PVA/SPTA, (d) PVA/P(SS-MA), (e) PEI/TMC and (f) PEI/P(SS-MA) under nitrogen atmosphere.

the films, though it's also possible that small molecules were volatilizing due to the presence of OH, SO$_3$H, NH$_2$, and CH$_2$ [17,27,28], the latter process in TGA exhibits a wider temperature range (160–330 °C). The homopolymer melting points as physical transition and the degradation temperatures of those substances led to the films' reduced thermal stability in the 330 °C–450 °C temperature range. The PVA/SPTA films had a lower mass loss rate than the other films in the 240–400 °C temperature range, demonstrating that the crosslinking network improved the PVA/SPTA films' thermostability. Consequently, increasing weight loss values throughout the decomposition phase show that there is proof of a chemical breakdown process that breaks chemical bonds in the material's main chain. Therefore, the larger temperature loss may have been due to the process by which the complete polymer breaks down into smaller pieces, whereas the smaller temperature loss may have been related to the bond disassociation of the ester or amide connections. Higher temperature drops have the biggest effect on weight loss, both in terms of rate and overall. The PEI/TMC materials exhibit two

degradation steps over the temperature range studied, while three distinct phases can be observed in the PEI/P(SS-MA) material. PEI with P(SS-MA) crosslinker undergoes thermal degradation through various processes influenced by the crosslinker. By limiting molecular activity and reducing the accessibility of polymer chains to thermal degradation pathways, crosslinking can improve the thermal durability of materials. P(SS-MA) crosslinker may alter the way PEI is degraded during thermal decomposition. Crosslinking can also promote the formation of thermally stable carbon residues, which act as a barrier against further degradation. In conclusion, the mechanism of chain breakage, carbon residue generation, and cross-linking events combined to lead to the thermal degradation of PEI with P(SS-MA) crosslinker.

3.3. Coating effects on surface structure

The surface morphology of the PVDF membrane was further analyzed using AFM, which demonstrated that surface roughness has a
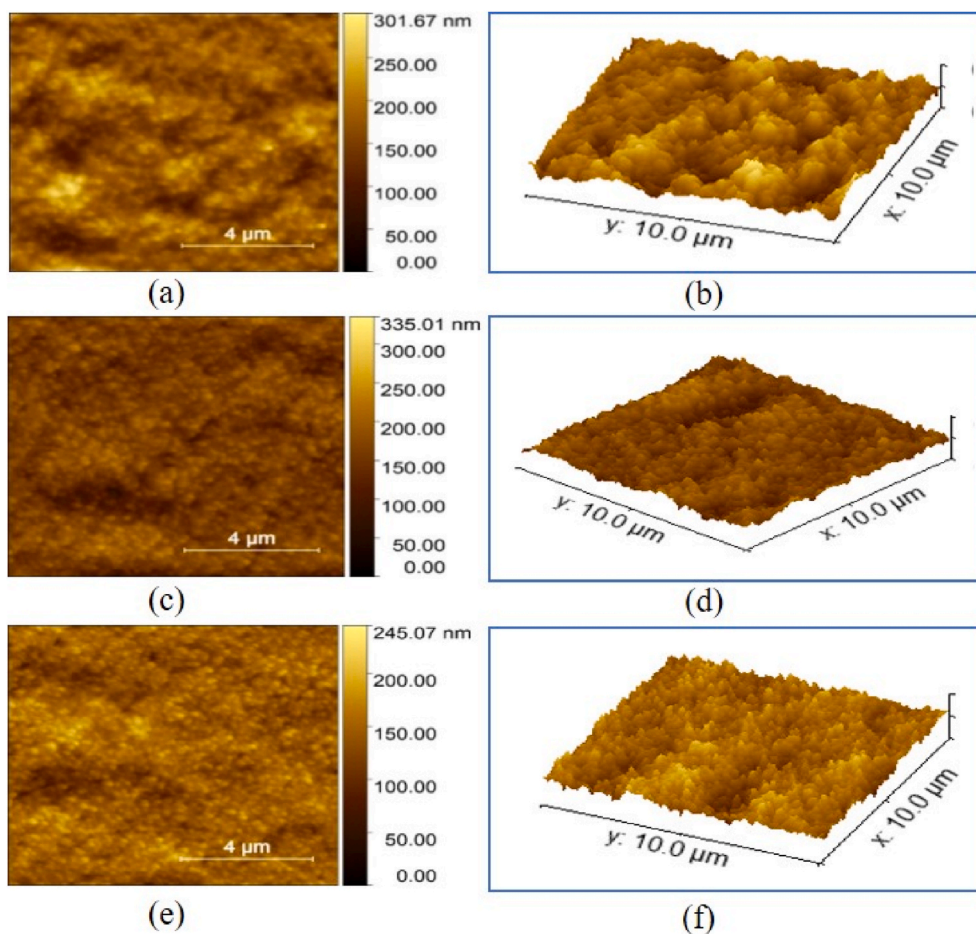
Fig. 8. The AFM images of the PVDF membrane. 2D and 3D surface morphology of substrate layer at room temperature (a, b) and 100 °C (c, d). 2D and 3D surface morphology of PEI/P(SS-MA)/PVDF composite membrane (e, f).
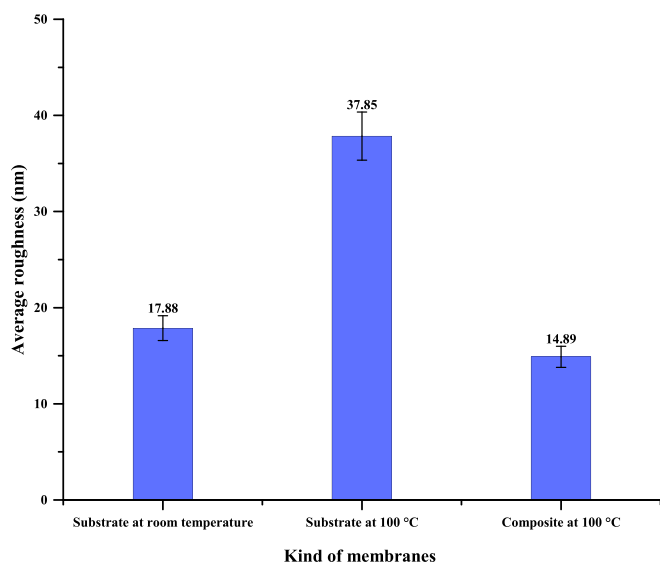

Fig. 9. Average roughness (nm) of substrate and composite membranes.

significant impact on desalination performance. The performance of the active layer of the prepared composite membrane is strongly influenced by the surface structure of the transition layer. The surface of the PVDF base layer was pretreated by two methods, preheating and surface pre-coating, respectively, after which the changes in the surface structure

were analyzed to measure the effects of different surface modification conditions on its surface roughness structure. According to Figs. 8 and 9, the average surface roughness of the PVDF substrate layer is 17.88 ± 1.3 nm at ambient temperature and 37.85 ± 2.5 nm at 100 °C. In addition, the PVDF membrane coating with PEI/P(SS-MA) has a surface roughness of 14.89 ± 1.1 nm. The composite membrane with PEI/P(SS-MA) has the lowest roughness value. The main factor was that the active layer PEI/P(SS-MA) was properly coated on top of the substrate layer. Smaller holes and better substrates are ideal for the intact coating of thin films. According to these results, the surface of the composite membrane made of PVDF was smoother.

The increased hydrophobicity of the PVDF substrate layer can significantly enhance pervaporation efficiency. AFM results indicate that the surface of the PVDF substrate membrane becomes increasingly rough over time. Consequently, this increased surface roughness contributes to the heightened hydrophobicity of the PVDF membrane.

An important feature of membranes is surface roughness, which affects the adsorption of surface substances and leads to membrane fouling [29]. Although the effect on fouling is less pronounced, membrane surface roughness has been shown to affect water transport and separation performance [30,31]. Fig. 9 shows that the average roughness of the PVDF/PEI/P(SS-MA) composite film is 14.89 ± 1.1 nm, while the average roughness of the PVDF support layer is 37.85 nm ± 2.5 at 100 °C. These results suggest that PVDF/PEI/P(SS-MA) composite membranes with low roughness values can reduce fouling and increase the high flux values. Additionally, the effectiveness of the pervaporation membrane is substantially influenced by the pore size and pore size distribution of the PVDF substrate, underscoring the importance of these
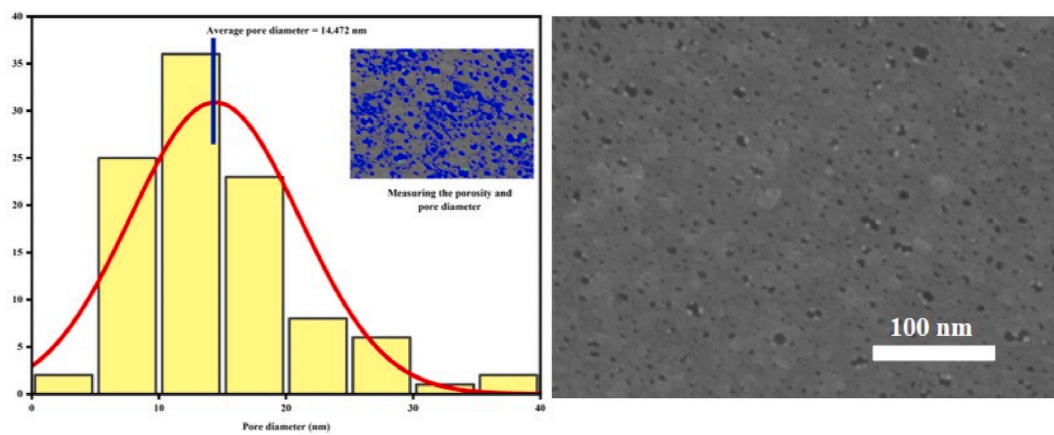
Fig. 10. Pore size distribution of the PVDF supporting layer.

Fig. 11. The surface morphology of the SEM images of membranes (1 μm). (a) PVDF supporting layer (a) and composite membranes with various active layers (b) PEI/TMC, (c) PVA/P(AA-AMPS), (d) PVA/SPTA, (e) PVA/P(SS-MA), & (f) PEI/P(SS-MA).
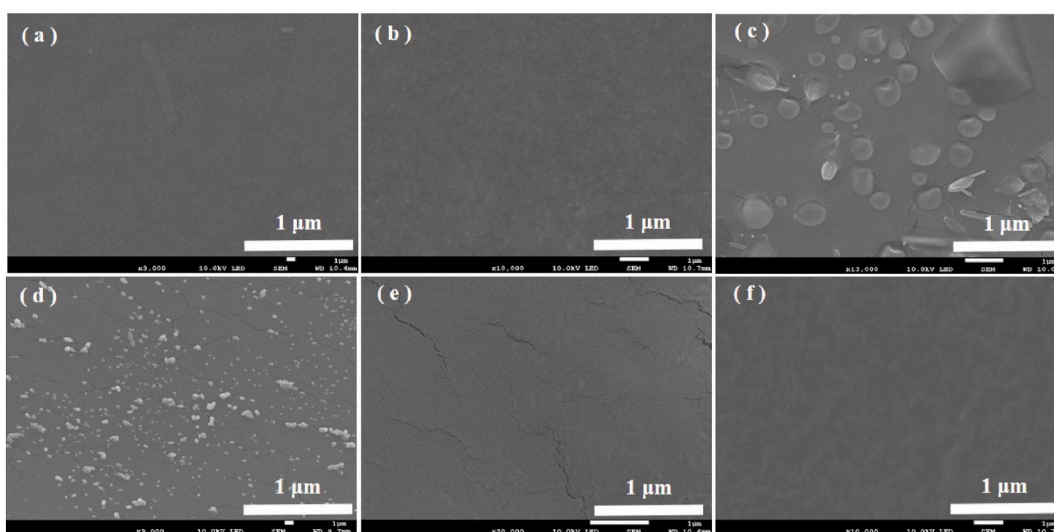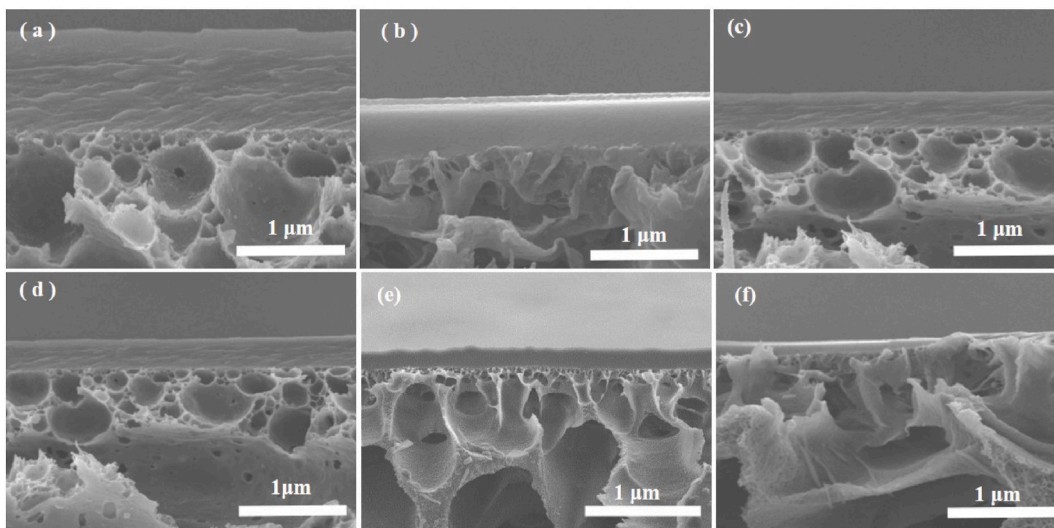

Fig. 12. The cross-section morphology of the SEM images of membranes (a) PVDF supporting layer and composite membranes with various active layers (b) PEI/P(SS-MA), (c) PVA/P(AA-AMPS), (d) PVA/SPTA, (e) PVA/P(SS-MA), & (f) PEI/TMC.

parameters in optimizing membrane performance. The SEM image of the PVDF substrate's bottom surface reveals a ridge and valley structure that enhances its hydrophobicity.

3.4. Characterization of porous structure in composite membranes

Scanning electron microscope (SEM) images are shown in Figs. 11 and 12 to illustrate the top surface and cross sections of the PVDF substrate and composite membranes. We spray the PVA and PEI coating solution directly onto the membrane surfaces using various crosslinking agents. It is easy to prepare a thin selective layer on the PVDF membrane due to its smaller average pore size. The PVDF substrate film, as shown in the picture, has many uniform holes and a uniform surface shape. The surface morphology of the PVDF substrate and the composite membranes did not have any defects. The cross-section morphology of all membranes has a traditional "ridge and valley" shape. The PVDF substrate layer had an average pore diameter of 14.472 ± 1.3 nm and a porosity of 46.178 ± 2.4 % according to Fig. 10.

In this experiment, a dead-end ultrafiltration system that was developed in the lab was used to assess the flux of pure water across the PVDF supporting membrane. The PVDF membrane's water flux was 73.37 ± 4.5 kg m^{-2} h^{-1}. We also examined the membranes' gas permeances using a gas permeance apparatus to replicate the passage of water vapor through them. The membrane's considerable thickness prevents the passage of gas. The gas permeability of the PVDF supporting layer was found to be high with nitrogen and carbon dioxide permeability values of 61.898 × 10^3 L m^{-2} h^{-1} and 52.423 × 10^3 L m^{-2} h^{-1}, respectively.

3.5. Analysis of membrane hydrophilicity

The water contact angles of various membranes were measured using the contact angle measurement device, and Fig. 13 shows that composite membranes containing PEI coating layers have lower contact angles and greater hydrophilicity than other membranes. Hydrophilic functional groups make the membrane surface more permeable due to the amide connection between PEI and P(SS-MA). Moreover, the relationship between surface roughness and water contact angle is shown in Fig. 14. As a result, a composite membrane made of PEI/P(SS-MA) has a decreased contact angle and exhibits enhanced water permeability.

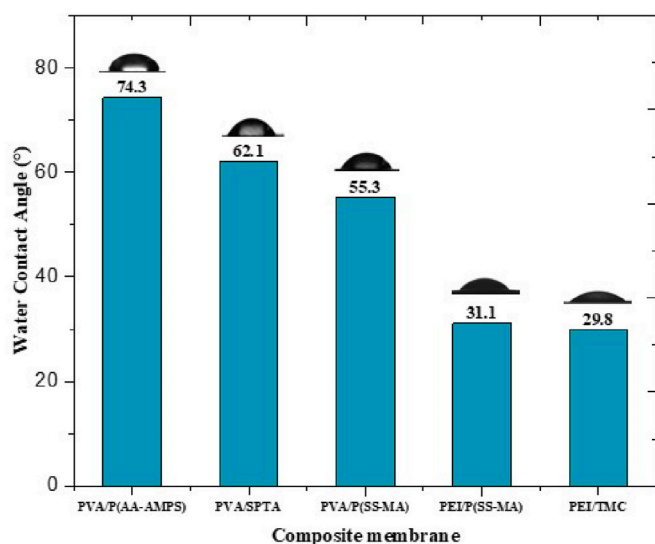Table 2 details the calculated degrees of swelling for the membranes,

Fig. 13. Water contact angle of PVDF composite membranes with different crosslinkers.

providing a comprehensive overview of their swelling behavior. There is a direct correlation between the membrane's swelling degree and the water diffusion coefficient; as the swelling degree decreases, so does the water diffusion coefficient. In a solution with 0 wt% salt (containing only deionized water), the swelling of the PEI-based membrane increases significantly. This phenomenon can be attributed to the substantial interaction between water molecules and the NH$_2$ groups in the PEI-based membranes, underscoring the hydrophilic nature of these membranes. Consequently, the hydrophilic coating of PEI is crucial in its capacity to absorb water. The ester bond between PVA and crosslinkers was created by the reaction between P(SS-MA), P(AA-AMPS), and SPTA functional groups. The esterification conversion was increased in this step using an acid catalyst (H$_2$SO$_4$, pH −1) and a high crosslinking temperature (100 °C). In this work, PEI and TMC, PEI, and P(SS-MA)) amides were achieved by condensation of the carboxylic acid groups (-COOH) of TMC, P(SS-MA) without a catalyst, and PEI amine groups (-NH$_2$). The amide bond between PEI and P(SS-MA) was confirmed by a crosslinking temperature of 100 °C. Intermolecular hydrogen bonding can also occur in these amide bonds. The film stiffened as a result of hydrogen bonding, which increased water flow. Hydrogen bonding plays a role in the performance of the composite membrane [32,33]. The performance of the composite films was later improved by a sulfonyl group (SO$_3$H), which increased the mechanical stability and water permeability of the films [34,35]. Amide bonds were one of the most important processes in the membrane. A key component in the preparation of synthetic membranes for desalination is the amide functional group. Because it can improve both the hydrophilicity of the film surface and its thermal stability [36,37]. In addition, surface hydrophilicity is considered one of the most important variables when evaluating water and salt transport properties. By using a membrane with excellent hydrophilic properties, the membrane performance was improved and the highest water flow value was achieved. In this study, the effectiveness of crosslinkers with different PVA and PEI polymers, including P(SS-MA), P(AA-AMPS), SPTA, and TMC, was tested. PVA/P(SS-MA) and PEI/P(SS-MA) showed the highest current values among them. P(SS-MA) was thus a better crosslink in this experiment. Amine groups, branched chains, and repeating units CH$_2$CH$_2$ are components of the polymer polyethyleneimine (PEI), a cationic hydrophilic polymer. The primary amine group of the PEI (NH$_2$) and acid group of P(SS-MA) can rapidly react to form an amide bond.

3.6. Pervaporation test for PVDF composite membrane

A 3.5 wt% NaCl solution was utilized as the feed to evaluate the pervaporation desalination performance of various PVDF composite membranes incorporating different crosslinkers at 72 °C. As depicted in Fig. 15 (a), it was observed that the PVDF composite membrane with PEI/P(SS-MA) exhibited superior membrane flux. In contrast, the PVDF/PEI/TMC composite membrane demonstrated lower water flux. This discrepancy is primarily attributed to the dense layer of the PEI/P(SS-MA) membrane, which possesses lower mass transfer resistance compared to the dense layers of the other composite membranes. Fig. 15 (a) and (b) illustrate that all composite membranes achieved salt rejections exceeding 99.9 %, indicating that their skin layers are nearly defect-free. The PEI/P(SS-MA) composite membrane displays significantly higher intrinsic water transport properties than the other composite membranes. The pervaporation desalination performance of PVDF/PEI/P(SS-MA) composite membranes is depicted in Fig. 15 (b), illustrating the relationship between feed temperature and process efficiency. The minimum observed water flux was 148.89 ± 5.6 kg m^{-2} h^{-1} at 42 °C, accompanied by a salt rejection rate of 99.97 %. Conversely, the maximum water flux reached 308.7 ± 13.8 kg m^{-2} h^{-1} at 72 °C, with a slightly lower salt rejection rate of 99.94 %. The data indicate that water flux values for PVDF/PEI/P(SS-MA) composite membranes increased with rising temperature. This trend can be attributed to the enhanced diffusivity of water at elevated temperatures,
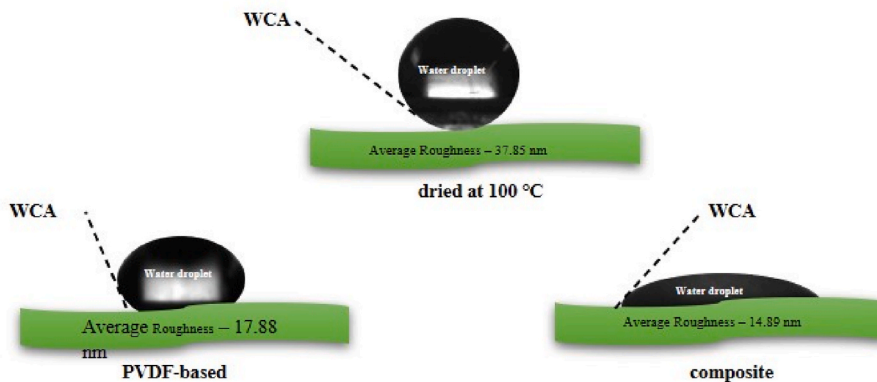
Fig. 14. Relationship between surface roughness and water contact angle.
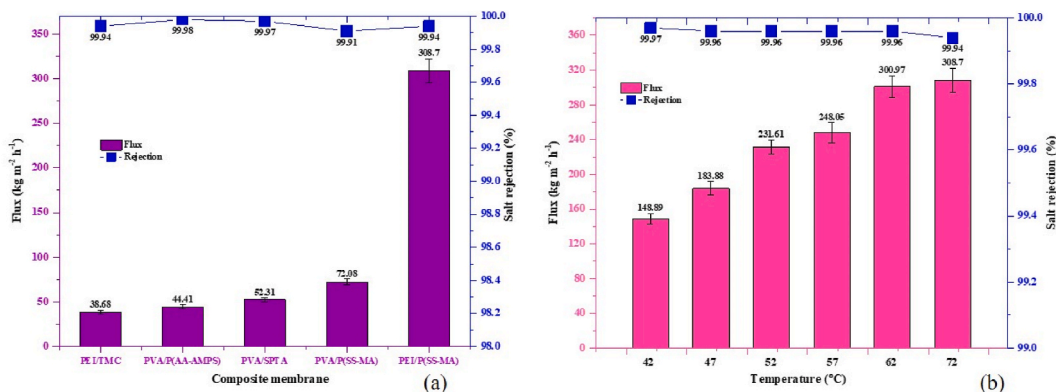

Fig. 15. (a) Desalination performance of PVDF composite membranes with various active layers at 72 °C, (b) Desalination performance of PVDF/PEI/P(SS-MA) composite membrane at different temperatures (42, 47, 52, 57, 62 & 72 °C).

which subsequently amplifies both the driving force for water transport and its force of movement.

3.7. Effects of temperature and salt concentration on the desalination properties

The performance of PVDF composite membranes in pervaporation desalination was assessed across various temperatures using a 3.5 wt% NaCl solution as the feed. The water flux of these membranes demonstrated a notable increase with rising feed temperature. Fig. 15 (b) demonstrates how the water flux of PVDF composite membranes increases from $148.89 \pm 6.1 \, kg \, m^{-2} \, h^{-1}$ to $308.7 \pm 13.8 \, kg \, m^{-2} \, h^{-1}$ as the feed temperature rises from 42 °C to 72 °C. This enhancement can be attributed to both the direct relationship between temperature and permeability, as well as the Arrhenius relationship governing the temperature dependency of membrane flux. Lower feed temperatures decrease fluidity and permeability while higher feed temperatures increase the partial pressure of water vapor at the feed side, improving the

water-driving force of the transferring composite membrane [18,27]. Consequently, a minor quantity of salt precipitated at the base of the membrane, potentially attributable to the swelling of the thin PEI/P(SS-MA) layer at elevated temperatures, leading to diminished salt rejection. The salt rejection rates for thin film composite membranes with PEI/P(SS-MA) layers also remained consistently above 99.9 %. The PVDF/PEI/P(SS-MA) composite membrane exhibited excellent desalination performance across a temperature range of 42 °C–72 °C using a 3.5 wt% NaCl feed solution. Fig. 16 demonstrates the superior performance of our membrane compared to all other composite PV desalination membranes manufactured via non-solvent-induced phase separation, achieving the highest possible levels of water flux [3,38]. This experiment demonstrated that the composite PVDF/PEI/P(SS-MA) membrane exhibits reduced salt rejection but increased vapor transport, attributed to its heightened permeability, especially at elevated temperatures. This feature makes it advantageous for testing highly concentrated brine solutions using PV desalination techniques. During this experiment, the desalination efficacy of the PVDF composite
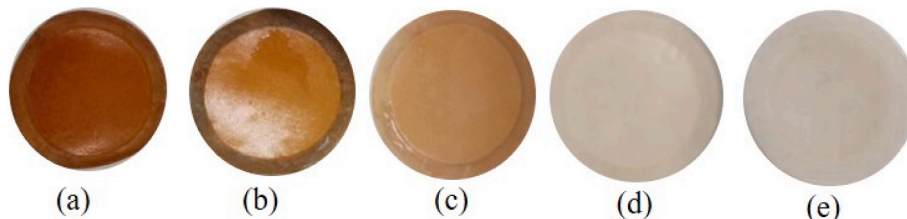

Fig. 16. Surface image of the PVDF composite membranes with different crosslinkers after desalination performance at 72 °C (a) PVA/P(SS-MA), (b) PVA/SPTA, (c) PVA/P(AA-AMPS), (d) PEI/TMC, & (e) PEI/P(SS-MA).
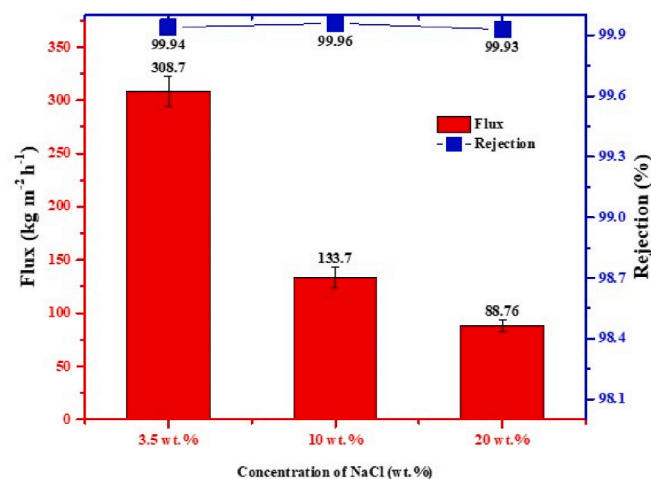
Fig. 17. Desalination performance of PVDF composite membranes with various weight percent of NaCl at 72 °C (3.5 wt %, 10 wt % and 20 wt %).
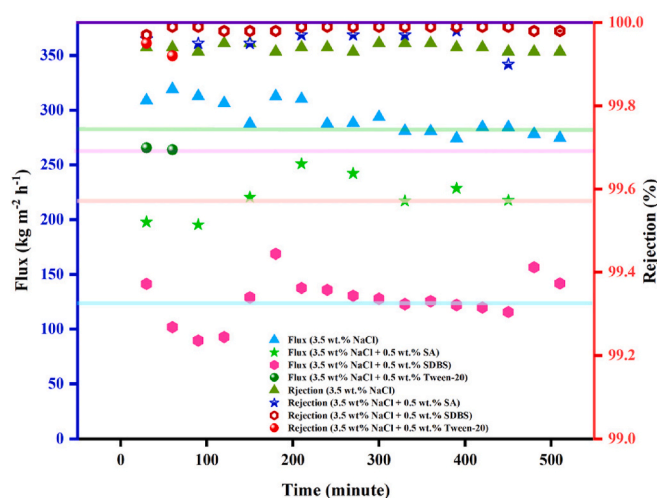

Fig. 18. The long-term operation stability of the PVDF/PEI composite membrane with P(SS-MA) crosslinker when treating a 3.5 wt % NaCl solution and a 3.5 wt % NaCl solution with 0.5 wt % Tween 20 or sodium dodecyl benzene sulfonate (SDBS) or sodium alginate (SA) acting as an organic foulant in the feed solution at 75 °C.

membrane was assessed by subjecting it to highly concentrated salt solutions, especially 3.5 wt%, 10 wt%, and 20 wt% NaCl, utilizing the pervaporation method at a temperature of 72 °C. The water flux considerably decreases from 308.7 ± 13.8 kg m^{-2} h^{-1} to 88.76 ± 5.4 kg m^{-2} h^{-1} at 72 °C when the concentration of NaCl rises from 3.5 wt % to 20 wt %, as shown in Fig. 17. As the salt solution's concentration rises, solute molecules increasingly occupy membrane surface sites, leading to a decrease in flux values. The primary factors driving this decline include the reduction in saturated vapor pressure due to the elevated salt content, thereby diminishing the driving force for mass transfer [39,40].

3.8. Long-term and antifouling performance of PVDF composite membranes

Table 3 details the characteristic properties of the foulant and surfactant employed in this experiment, providing essential insights into their roles and behaviors during the study. Furthermore, Fig. 18 shows the long-term saltwater extraction capability and antifouling properties of the PVDF composite membranes. After 510 min, 800 mL of fresh water was extracted from a 3.5 wt% NaCl solution using a PVDF composite membrane with an effective area of 3.14×10^{-4} m^2 at 75 °C, resulting in a water flux of 284.5 kg m^{-2} h^{-1}. When the feed solution containing 0.5 wt% of the anionic surfactant (SDBS) was used with 3.5 wt% sodium chloride, the PVDF composite membrane achieved a water flux of 220.45 kg m^{-2} h^{-1}. Throughout the study, the salt rejections consistently surpassed 99.9 % at both the initial and final stages of the test. Long-term desalination testing with PVDF composite membrane using Tween-20, a non-ionic surfactant, was found to be impractical. The findings indicated that the PVDF layer was more effective in

preventing pore-clogging caused by SA and SDBS compared to non-ionic Tween-20 surfactants. There has been a reduction in water flux as a result of the possible cake layer that developed on the PVDF composite layer surface. Preventing the formation of a cake layer on the surface of the coating layer during prolonged desalination tests remains challenging. However, the PVDF composite membrane demonstrates remarkable long-term operational stability, as indicated by the robust adhesive connection observed at the interface between the PEI and PVDF substrate. In addition, Table 4 offers a detailed comparative analysis of desalination performance under various conditions for membrane materials. These materials were prepared by different research teams, providing a comprehensive overview of their effectiveness and highlighting the advancements made in membrane technology across diverse research efforts.

4. Conclusion

This study outlines the development of high-performance PV membranes, achieved by applying a hydrophilic coating layer of PEI onto a hydrophobic substrate surface. The resultant PV composite membranes exhibited substantial salt rejection alongside enhanced water permeance simultaneously. Furthermore, a thorough investigation was conducted into the role of the supporting layers. The PVDF substrate featured numerous small pores. High-performance PVDF composite membranes were manufactured and assessed by spray-coating polymer solutions

Table 3
Characteristic properties of foulant and surfactant.

Foulant Name	Type	Formula	Chemical structure
Sodium alginate (SA)	Sodium salt of alginic acid (polysaccharide, Bio foulant)	$(C_6H_7NaO_6)_n$	
Sodium dodecyl benzene sulfonate (SDBS)	Sodium salt of linear alkyl benzene sulfonate (Anionic surfactant)	$C_{18}H_{29}NaO_3S$	
Tween 20	Polysorbate type (non-ionic surfactant)	$C_{26}H_{50}O_{10}$	

Table 4
Pervaporation desalination performance of different membranes.

Membrane ID	Feed solution (NaCl, wt.%)	Temperature (°C)	Flux (kg m^{-2} h^{-1})	Salt rejection (%)	Ref:
PEI/PVDF	3.5	72	308.7	99.94	This experiment
GO-PVA/PVDF	10	65	28	>99.9	[41]
PVA-SBQ/NC-PAN	3.5	75	122.6	99.9	[19]
PVA-PSU hollow fiber	3	71	7.4	99.9	[28]
PVA-PAN	3.5	70	46.3	99.8	[17]
PVA/NC-PAN	3.5	80	238.65	99.8	[21]
PVA/PTFE	3.5	75	143.4	99.9	[42]
G.O/ceramic	35	75	32.1	99.7	[4]
PVA-FS/PVDF	3.5	70	34	99.93	[22]
PVA/PTFE	3.5	75	143	–	[42]
GO/PI MMM	3.5	90	36.1	99.8	[43]
GO/PAN	3.5	90	65.1	99.8	[26]
PVA-MA-SiO$_2$	0.2	22	6.93	99.5	[43]
SPEEK/PES	7.0	70	5.73	99.99	[44]

with various crosslinkers onto the PVDF ultrafiltration membrane. The introduction of PEI/P(SS-MA) enhanced the hydrophilicity, morphology, and surface smoothness of the composite membrane. The amide links within PEI and P(SS-MA) contributed to improving water permeability. At 72 °C, the water flux through the composite PVDF/PEI/P(SS-MA) membrane reached 308.7 ± 13.8 kg m^{-2} h^{-1}. Our research highlights the active layer as a crucial component of PV membranes in desalination. Consequently, utilizing PEI/P(SS-MA) as the active layer on a PVDF substrate led to an increase in water flux, attributed to the anti-trade-off effect. Compared to alternative composite membranes, the PVDF/PEI/P(SS-MA) composite membrane demonstrates a smoother, less impaired surface structure and enhanced water flux permeability. The membrane's performance can also be influenced by the crosslinker, which undoubtedly plays a crucial role. These findings indicate that the PVDF/PEI/P(SS-MA) composite membrane holds promise for long-term applications in desalination or wastewater treatment.

CRediT authorship contribution statement

Thi Thi Mar: Writing – review & editing, Writing – original draft, Visualization, Software, Methodology, Investigation, Formal analysis, Data curation, Conceptualization. **Yunlong Xue:** Resources, Methodology, Formal analysis, Data curation, Conceptualization. **Yu Chang:** Formal analysis, Data curation, Conceptualization. **Zijian Yu:** Software, Data curation, Conceptualization. **Zhongxiao Du:** Software, Data curation, Conceptualization. **Bing Cao:** Writing – review & editing, Writing – original draft, Visualization, Validation, Supervision, Resources, Project administration, Methodology, Investigation, Formal analysis, Conceptualization. **Rui Zhang:** Writing – review & editing, Writing – original draft, Visualization, Validation, Supervision, Project administration, Methodology, Investigation, Formal analysis, Conceptualization.

Declaration of competing interest

The authors declare that they have no known competing financial interests or personal relationships that could have appeared to influence the work reported in this paper.

Data availability

Data will be made available on request.

References

[1] W. Chen, S. Chen, T. Liang, Q. Zhang, Z. Fan, H. Yin, K.W. Huang, X. Zhang, Z. Lai, P. Sheng, High-flux water desalination with interfacial salt sieving effect in nanoporous carbon composite membranes, Nat. Nanotechnol. 13 (4) (2018) 345–350, https://doi.org/10.1038/s41565-018-0067-5.

[2] B. Liang, K. Pan, L. Li, E.P. Giannelis, B. Cao, High performance hydrophilic pervaporation composite membranes for water desalination, Desalination 347 (2014) 199–206, https://doi.org/10.1016/j.desal.2014.05.021.

[3] Q. Li, B. Cao, P. Li, Fabrication of high performance pervaporation desalination composite membranes by optimizing the support layer structures, Ind. Eng. Chem. Res. 57 (32) (2018) 11178–11185, https://doi.org/10.1021/acs.iecr.8b02505.

[4] K. Xu, B. Feng, C. Zhou, A. Huang, Synthesis of highly stable graphene oxide membranes on polydopamine functionalized supports for seawater desalination, Chem. Eng. Sci. 146 (2016) 159–165, https://doi.org/10.1016/j.ces.2016.03.003.

[5] M. Mukherjee, S. Roy, K. Bhowmick, S. Majumdar, I. Prihatiningtyas, B. Van der Bruggen, P. Mondal, Development of high performance pervaporation desalination membranes: a brief review, Process Saf. Environ. Protect. 159 (2022) 1092–1104, https://doi.org/10.1016/j.psep.2022.01.076.

[6] S. Subaer, H. Fansuri, A. Haris, M. Misdayanti, I. Ramadhan, T. Wibawa, Y. Putri, H. Ismayanti, A. Setiawan, Pervaporation membranes for seawater desalination based on Geo–rGO–TiO2 nanocomposites: Part 2—membranes performances, Membranes 12 (11) (2022) 1046–1061, https://doi.org/10.3390/membranes12111046.

[7] I. Prihatiningtyas, B. Van der Bruggen, Nanocomposite pervaporation membrane for desalination, Chem. Eng. Res. Des. 164 (2020) 147–161, https://doi.org/10.1016/j.cherd.2020.10.005.

[8] M. Li, L. Wu, C. Zhang, W. Chen, C. Liu, Hydrophilic and antifouling modification of PVDF membranes by one-step assembly of tannic acid and polyvinylpyrrolidone, Appl. Surf. Sci. 483 (2019) 967–978, https://doi.org/10.1016/j.apsusc.2019.04.057.

[9] G. Amy, N. Ghaffour, Z. Li, L. Francis, R.V. Linares, T. Missimer, S. Lattemann, Membrane-based seawater desalination: present and future prospects, Desalination 401 (2017) 16–21, https://doi.org/10.1016/j.desal.2016.10.002.

[10] T. Eljaddi, D.L.M. Mendez, E. Favre, D. Roizard, Development of new pervaporation composite membranes for desalination: theoretical and experimental investigations, Desalination 507 (2021) 115006–115015, https://doi.org/10.1016/j.desal.2021.115006.

[11] D. Li, H. Wang, Recent developments in reverse osmosis desalination membranes, J. Mater. Chem. 20 (22) (2010) 4551–4566, https://doi.org/10.1039/b924553g.

[12] T. Miyoshi, M. Hayashi, K. Shimamura, H. Matsuyama, Important fractions of organic matter causing fouling of seawater reverse osmosis (SWRO) membranes, Desalination 390 (2016) 72–80, https://doi.org/10.1016/j.desal.2016.03.020.

[13] R.A. Maltos, J. Regnery, N. Almaraz, S. Fox, M. Schutter, T.J. Cath, M. Veres, B. D. Coday, T.Y. Cath, Produced water impact on membrane integrity during extended pilot testing of forward osmosis – reverse osmosis treatment, Desalination 440 (2018) 99–110, https://doi.org/10.1016/j.desal.2018.02.029.

[14] S.S. Shenvi, A.M. Isloor, A.F. Ismail, A review on RO membrane technology: developments and challenges, Desalination 368 (2015) 10–26, https://doi.org/10.1016/j.desal.2014.12.042.

[15] E. Halakoo, X. Feng, Layer-by-layer assembly of polyethyleneimine/graphene oxide membranes for desalination of high-salinity water via pervaporation, Sep. Purif. Technol. 234 (2020) 116077–116088, https://doi.org/10.1016/j.seppur.2019.116077.

[16] H.F.M. Austria, R.L.G. Lecaros, W.-S. Hung, L.L. Tayo, C.-C. Hu, H.-A. Tsai, K.-R. Lee, J.-Y. Lai, Investigation of salt penetration mechanism in hydrolyzed

polyacrylonitrile asymmetric membranes for pervaporation desalination, Desalination 463 (2019) 32–39, https://doi.org/10.1016/j.desal.2019.04.012.

[17] B. Liang, Q. Li, B. Cao, P. Li, Water permeance, permeability and desalination properties of the sulfonic acid functionalized composite pervaporation membranes, Desalination 433 (2018) 132–140, https://doi.org/10.1016/j.desal.2018.01.028.

[18] D.D. Kachhadiya, Z.V.P. Murthy, Graphene oxide modified CuBTC incorporated PVDF membranes for saltwater desalination via pervaporation, Sep. Purif. Technol. 290 (2022) 120888–120899, https://doi.org/10.1016/j.seppur.2022.120888.

[19] J. Meng, P. Zhao, B. Cao, C.H. Lau, Y. Xue, R. Zhang, P. Li, Fabricating thin-film composite membranes for pervaporation desalination via photo-crosslinking, Desalination 512 (2021) 115128–115136, https://doi.org/10.1016/j.desal.2021.115128.

[20] N.D. Hilmioglu, F.U. Nigiz, Pervaporative desalination of seawater using a polyvinylidene fluoride based membrane, Water Supply 18 (5) (2018) 1674–1681, https://doi.org/10.2166/ws.2017.228.

[21] D. Qin, R. Zhang, B. Cao, P. Li, Fabrication of high-performance composite membranes based on hierarchically structured electrospun nanofiber substrates for pervaporation desalination, J. Membr. Sci. 638 (2021) 119672–119682, https://doi.org/10.1016/j.memsci.2021.119672.

[22] P. Zhao, Y. Xue, R. Zhang, B. Cao, P. Li, Fabrication of pervaporation desalination membranes with excellent chemical resistance for chemical washing, J. Membr. Sci. 611 (2020) 118367–118376, https://doi.org/10.1016/j.memsci.2020.118367.

[23] Y.L. Xue, J. Huang, C.H. Lau, B. Cao, P. Li, Tailoring the molecular structure of crosslinked polymers for pervaporation desalination, Nat. Commun. 11 (1) (2020) 1461–1469, https://doi.org/10.1038/s41467-020-15038-w.

[24] J. Wang, B. Cao, R. Zhang, P. Li, Spray-coated tough thin film composite membrane for pervaporation desalination, Chem. Eng. Res. Des. 179 (2022) 493–501, https://doi.org/10.1016/j.cherd.2022.01.028.

[25] D. Qin, H. Liu, T. Xiong, J. Wang, R. Zhang, B. Cao, P. Li, Enhancing the property of composite pervaporation desalination membrane by fabricating a less resistance substrate with porous but skinless surface structure, Desalination 525 (2022) 115496–115505, https://doi.org/10.1016/j.desal.2021.115496.

[26] B. Liang, W. Zhan, G. Qi, S. Lin, Q. Nan, Y. Liu, B. Cao, K. Pan, High performance graphene oxide/polyacrylonitrile composite pervaporation membranes for desalination applications, J. Mater. Chem. A 3 (9) (2015) 5140–5147, https://doi.org/10.1039/c4ta06573e.

[27] G. Liu, J. Shen, Q. Liu, G. Liu, J. Xiong, J. Yang, W. Jin, Ultrathin two-dimensional MXene membrane for pervaporation desalination, J. Membr. Sci. 548 (2018) 548–558, https://doi.org/10.1016/j.memsci.2017.11.065.

[28] S.G. Chaudhri, B.H. Rajai, P.S. Singh, Preparation of ultra-thin poly(vinyl alcohol) membranes supported on polysulfone hollow fiber and their application for production of pure water from seawater, Desalination 367 (2015) 272–284, https://doi.org/10.1016/j.desal.2015.04.016.

[29] O. Agboola, E.R. Sadiku, P. Popoola, O.S.I. Fayomi, A.O. Ayeni, D.T. Dick, A. T. Adegbola, L. Moropeng, M. Ramakhokhovhu, Surface roughness of ternary blends: polypropylene/chitosan/sisal fiber membranes, Mater. Today: Proc. 38 (2021) 2342–2346, https://doi.org/10.1016/j.matpr.2020.06.513.

[30] M.I. Baig, P.G. Ingole, J.-d. Jeon, S.U. Hong, W.K. Choi, B. Jang, H.K. Lee, Water vapor selective thin film nanocomposite membranes prepared by functionalized Silicon nanoparticles, Desalination 451 (2019) 59–71, https://doi.org/10.1016/j.desal.2017.06.005.

[31] Z. Zhong, D. Li, B. Zhang, W. Xing, Membrane surface roughness characterization and its influence on ultrafine particle adhesion, Sep. Purif. Technol. 90 (2012) 140–146, https://doi.org/10.1016/j.seppur.2011.09.016.

[32] N. Zhang, S. Chen, B. Yang, J. Huo, X. Zhang, J. Bao, X. Ruan, G. He, Effect of hydrogen-bonding interaction on the arrangement and dynamics of water confined in a polyamide membrane: a molecular dynamics simulation, J. Phys. Chem. B 122 (17) (2018) 4719–4728, https://doi.org/10.1021/acs.jpcb.7b12790.

[33] R.M. Madero-Castro, S. Calero, A.O. Yazaydin, The role of hydrogen bonding in the dehydration of bioalcohols in hydrophobic pervaporation membranes, J. Mol. Liq. 340 (2021) 117297–117302, https://doi.org/10.1016/j.molliq.2021.117297.

[34] W. Jang, C. Lee, S. Sundar, Y.G. Shul, H. Han, Thermal and hydrolytic stability of sulfonated polyimide membranes with varying chemical structure, Polym. Degrad. Stabil. 90 (3) (2005) 431–440, https://doi.org/10.1016/j.polymdegradstab.2005.04.012.

[35] F.L. Moruno, J.E. Rubio, P. Atanassov, J.M. Cerrato, C.G. Arges, C. Santoro, Microbial desalination cell with sulfonated sodium poly(ether ether ketone) as cation exchange membranes for enhancing power generation and salt reduction, Bioelectrochemistry 121 (2018) 176–184, https://doi.org/10.1016/j.bioelechem.2018.02.004.

[36] B. Gadgil, P. Damlin, E. Dmitrieva, T. Ääritalo, C. Kvarnström, Exploring amide linkage in a polyviologen derivative towards simultaneous voltammetric determination of Pb(II), Cu(II) and Hg(II) ions, Electrochim. Acta 192 (2016) 482–488, https://doi.org/10.1016/j.electacta.2016.02.006.

[37] V. Freger, G.Z. Ramon, Polyamide desalination membranes: formation, structure, and properties, Prog. Polym. Sci. 122 (2021) 101451–101484, https://doi.org/10.1016/j.progpolymsci.2021.101451.

[38] L. Li, J. Hou, Y. Ye, J. Mansouri, V. Chen, Composite PVA/PVDF pervaporation membrane for concentrated brine desalination: salt rejection, membrane fouling and defect control, Desalination 422 (2017) 49–58, https://doi.org/10.1016/j.desal.2017.08.011.

[39] Y. Song, F. Pan, Y. Li, K. Quan, Z. Jiang, Mass transport mechanisms within pervaporation membranes, Front. Chem. Sci. Eng. 13 (3) (2019) 458–474, https://doi.org/10.1007/s11705-018-1780-1.

[40] P. Schaetzel, R. Bouallouche, H. Aït Amar, Q.T. Nguyen, B. Riffault, S. Marais, Mass transfer in pervaporation: the key component approximation for the solution-diffusion model, Desalination 251 (1–3) (2010) 161–166, https://doi.org/10.1016/j.desal.2009.09.132.

[41] L. Li, J. Hou, Y. Ye, J. Mansouri, Y. Zhang, V. Chen, Suppressing salt transport through composite pervaporation membranes for brine desalination, Appl. Sci. 7 (8) (2017) 856–874, https://doi.org/10.3390/app7080856.

[42] J. Meng, C.H. Lau, Y. Xue, R. Zhang, B. Cao, P. Li, Compatibilizing hydrophilic and hydrophobic polymers via spray coating for desalination, J. Mater. Chem. A 8 (17) (2020) 8462–8468, https://doi.org/10.1039/d0ta00871k.

[43] B. Feng, K. Xu, A. Huang, Synthesis of graphene oxide/polyimide mixed matrix membranes for desalination, RSC Adv. 7 (4) (2017) 2211–2217, https://doi.org/10.1039/c6ra24974d.

[44] H. Zeng, S. Liu, J. Wang, Y. Li, L. Zhu, M. Xu, C. Wang, Hydrophilic SPEEK/PES composite membrane for pervaporation desalination, Sep. Purif. Technol. 250 (2020) 117265–117290, https://doi.org/10.1016/j.seppur.2020.117265.